Journal of Materials Chemistry C

ROYAL SOCIETY OF CHEMISTRY

PAPER

View Article Online
View Journal | View Issue

Cite this: J. Mater. Chem. C, 2023, 11, 16310

Upconversion enhancement through engineering the local crystal field in Yb^{3+} and Er^{3+} codoped $BaWO_4$ along with excellent temperature sensing performance†

Guotao Xiang, *[a] Zhen Liu,[a] Zhiyu Yang,[a] Yongjie Wang,[a] Lu Yao,[a] Sha Jiang,[a] Xianju Zhou,[a] Li Li,[a] Xiaojun Wang *[c] and Jiahua Zhang *[b]

Received 17th September 2023,
Accepted 8th November 2023

DOI: 10.1039/d3tc03386d

rsc.li/materials-c

High-efficiency upconversion (UC) luminescence has been a hot topic in the development of optical materials. In this study, an extremely strong green UC is successfully achieved in the $BaWO_4$:Yb^{3+}/Er^{3+} phosphor through engineering the local environment around the luminescent centers, realized by Ca^{2+} doping. The green UC intensity of Ca^{2+} doped $BaWO_4$:Yb^{3+}/Er^{3+} is 6.5 and 2.3 times stronger than that of $BaWO_4$:Yb^{3+}/Er^{3+} and $CaWO_4$:Yb^{3+}/Er^{3+}, respectively. Eu^{3+} ions are employed as the structure probe to detect the evolution of the crystal field symmetry with the increase of Ca^{2+} doping concentration, the results of which match well with the corresponding variation of the UC spectra. Meanwhile, the $BaWO_4$:Yb^{3+}/Er^{3+}/Ca^{2+} exhibits excellent temperature sensing performance based on the fluorescence intensity ratio (FIR) between the thermally coupled $^2H_{11/2}$ and $^4S_{3/2}$ states of Er^{3+} ions. Its absolute sensitivity and relative sensitivity for optical thermometry can reach 1.21% K^{-1} and 1.31% K^{-1}, outperforming the majority of the same type optical thermometers. The temperature resolution of the present thermometer remains lower than 0.1 K within the temperature range of 298 K to 573 K. The intense green UC luminescence along with the outstanding thermal properties makes the $BaWO_4$:Yb^{3+}/Er^{3+} phosphor a promising candidate for optical thermometry.

Introduction

Nowadays, a great deal of attention has been paid to develop efficient upconversion (UC) luminescent materials due to their unique optical properties of generating ultraviolet or visible light from the 4f electrons of rare-earth ions upon the excitation of near-infrared (NIR) light, contributing to great potential applications in the fields of solid state laser, biological medicine, anti-counterfeiting marker and so forth.[1,2] Thereinto, the selection of host materials plays a vitally important role in obtaining high-efficiency UC emission. The ideal host for intense UC luminescence should possess low enough phonon energy to meet the key requirement of reducing non-radiative consumption as much as possible. Up to now, fluorides are the most commonly used matrixes for UC studies in the previous literature reports, especially hexagonal $NaYF_4$ and $NaLuF_4$, which are deemed as the optimal UC hosts because of their extremely low phonon energy ($\sim$360 cm^{-1}).[3–11]

However, the poor chemical stability makes fluorides difficult to afford the further applications. By contrast, as an essential member of oxide family, tungstates AWO_4 (A = Ca, Sr, and Ba) with the scheelite crystal structure present remarkable optical properties along with excellent thermal and chemical stability, which makes them potential candidates for UC studies.[12–19] For instance, bright green UC emission is successfully realized in Yb^{3+} and Er^{3+} codoped $BaWO_4$ phosphors.[20] Nevertheless, the UC performance of $BaWO_4$:Yb^{3+}/Er^{3+} still needs to be modified and improved to satisfy more application demands. Actually, numerous research efforts have demonstrated that impure doping is an effective strategy for UC enhancement, resulting from the high sensitivity of the rare-earth ions to their surrounding crystal field.[21–24] More specifically, the optical transition probabilities of luminescent centers can be promoted through the destruction of crystal field symmetry, caused by ionic substitution. For example, the UC luminescence of $NaYF_4$:Yb^{3+}/Er^{3+} is greatly enhanced by Mo^{3+} doping, resulting from the decrease of the

[a] Department of Mathematics and Physics, Chongqing University of Posts and Telecommunications, 2 Chongwen Road, Chongqing 400065, China. E-mail: xianggt@cqupt.edu.cn
[b] State Key Laboratory of Luminescence and Applications, Changchun Institute of Optics, Fine Mechanics and Physics, Chinese Academy of Sciences, 3888 Eastern South Lake Road, Changchun 130033, China. E-mail: zhangjh@ciomp.ac.cn
[c] Department of Physics & Astronomy, Georgia Southern University, Statesboro, Georgia 30460, USA. E-mail: xwang@georgiasouthern.edu

† Electronic supplementary information (ESI) available. See DOI: https://doi.org/10.1039/d3tc03386d

local crystal field symmetry around the lanthanide ions.[25] However, to the best of our knowledge, the UC improvement of $BaWO_4$:Yb^{3+}/Er^{3+} through engineering local environment have been rarely investigated so far.

In this study, a high temperature solid state reaction method is used to synthesize the $BaWO_4$:Yb^{3+}/Er^{3+} phosphor. Through Ca^{2+} doping, the green UC intensity of the as-prepared sample is enhanced by a factor of 6.5 times due to the decrease of the local symmetry around the luminescent centers, which has been established using a Eu^{3+} structure probe. Moreover, the Ca^{2+} doped $BaWO_4$:Yb^{3+}/Er^{3+} phosphor presents remarkable temperature sensing performance based on the fluorescence intensity ratio (FIR) between the thermally coupled $^2H_{11/2}$ and $^4S_{3/2}$ levels of Er^{3+} ions, from which outstanding sensitivity and resolution for temperature sensing can be obtained. All the findings reveal that $BaWO_4$:Yb^{3+}/Er^{3+}/Ca^{2+} is an efficient UC material with superior optical thermometry ability.

Experimental

Chemicals

$CaCO_3$ (99.99%), WO_3 (99.99%) and Er_2O_3 (99.99%) are provided by Shanghai Aladdin Biochemical Technology Co., Ltd. $BaCO_3$ (99.99%) and Yb_2O_3 (99.99%) are obtained from China National Pharmaceutical Group Chemical Reagent Co., Ltd. The reagents are all utilized directly in the preparation section without additional purification.

Sample preparation

$BaWO_4$:x% Yb^{3+}/y% Er^{3+}/z% Ca^{2+} (x = 1, 5, 10, 20, 30, 40; y = 0.2, 0.5, 1, 2, 3, 4; z = 0, 1, 5, 10, 20) powders and $CaWO_4$:5% Yb^{3+}/1% Er^{3+} are synthesized *via* conventional high temperature solid state reactions. First of all, $BaCO_3$, $CaCO_3$, WO_3, Yb_2O_3 and Er_2O_3 are weighed based on the stoichiometric ratio and then homogenized by grinding with anhydrous ethanol in an agate mortar. After that, the ground precursors are calcinated at 1300 °C for 8 hours in a box-type furnace and then naturally cooled down to the ambient temperature.

Characterization

The structure of the powders is determined by using a powder X-ray diffractometer (XRD) supplied by Beijing Persee Analysis General Instrument Co., Ltd. An FLS 1000 spectrometer equipped with a 980 nm diode laser as the excitation source is employed to collect the spectral data. The sample temperature is controlled by using a HFS600E-PB2 temperature control device.

Results and discussion

Phase characterization

The XRD patterns of $BaWO_4$:x% Yb^{3+}/y% Er^{3+}/z% Ca^{2+} as well as $CaWO_4$:Yb^{3+}/Er^{3+} are recorded to examine the structure and phase purity of the prepared samples. As depicted in Fig. 1(a)

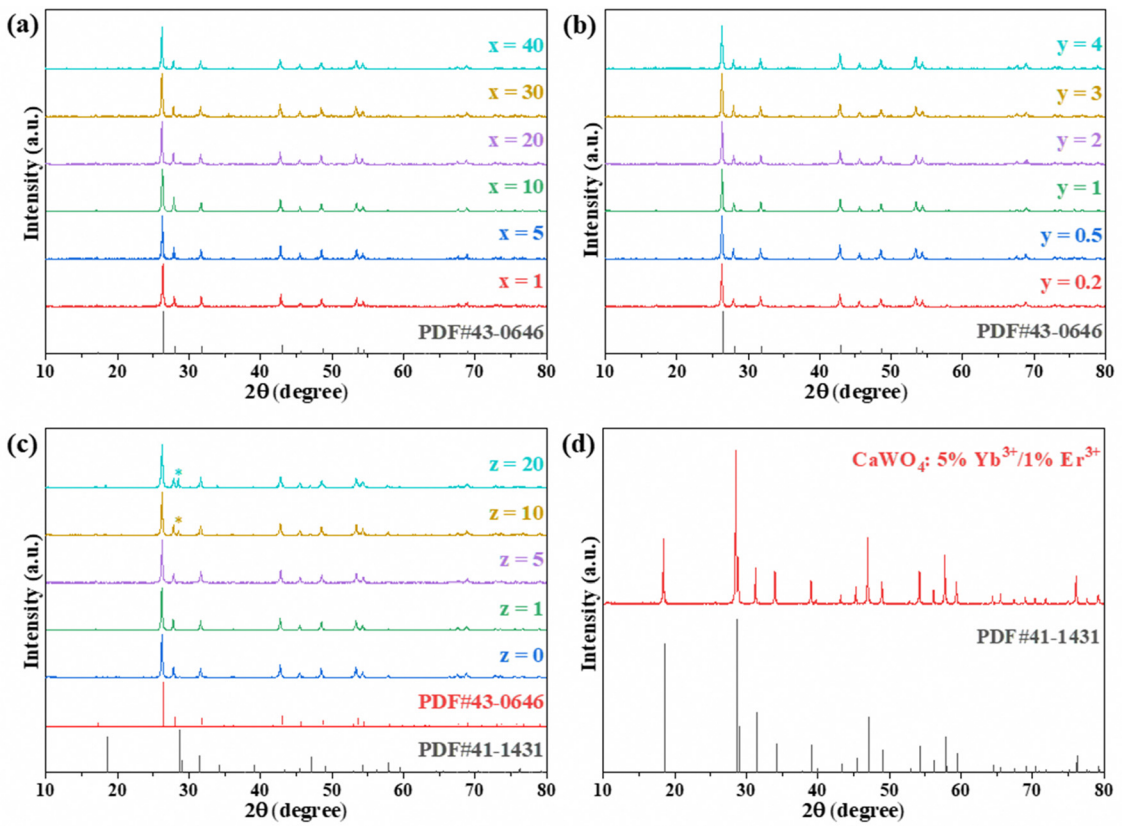

Fig. 1 The XRD patterns of (a) $BaWO_4$:x% Yb^{3+}/1% Er^{3+}, (b) $BaWO_4$:20% Yb^{3+}/y% Er^{3+}, (c) $BaWO_4$:10% Yb^{3+}/1% Er^{3+}/z% Ca^{2+} and (d) $CaWO_4$:5% Yb^{3+}/1% Er^{3+}.

and (b), all the diffraction peaks are well indexed by the standard tetragonal $BaWO_4$ with the space group $I4_1/a$ (JCPDS no. 43-0646). No additional peaks are observed, confirming the successful insertion of Yb^{3+} and Er^{3+} in the $BaWO_4$ matrix. Fig. 1(c) shows the XRD patterns of $BaWO_4$:10% Yb^{3+}/1% Er^{3+} doped with various Ca^{2+} concentrations. Definitely, the Ca^{2+} doping at low concentration has no effect on the phase purity of the samples, but a secondary crystalline phase corresponding to $CaWO_4$ (JCPDS no. 41-1431) appears when the Ca^{2+} doping concentration reaches 10%, of which the diffraction peaks have been marked by the asterisks. In addition, the synthesized $CaWO_4$:5% Yb^{3+}/1% Er^{3+} sample shows good agreement with the standard $CaWO_4$, as presented in Fig. 1(d).

Luminescence properties

UC performance

Fig. 2(a) and (b) show the UC spectra of $BaWO_4$ doped with different Yb^{3+} and Er^{3+} concentrations. Distinctly, two emission bands emerge in the range from 500 nm to 700 nm, all belonging to the devotion of Er^{3+} ions. Concretely, the strong green emission band is attributed to Er^{3+}:$^2H_{11/2} \rightarrow {}^4I_{15/2}$ transition located at 531 nm and Er^{3+}:$^4S_{3/2} \rightarrow {}^4I_{15/2}$ transition located at 553 nm, and the weak red emission band originates from Er^{3+}:$^4F_{9/2} \rightarrow {}^4I_{15/2}$ transition peaked at 656 nm. The variation of Yb^{3+} and Er^{3+} doping concentration has no distinct influence on the location and profile of the UC spectra. However, the spectral intensity is critically changed with the elevation of Yb^{3+} and Er^{3+} concentration, from which the optimal concentration of Yb^{3+} and Er^{3+} is determined to be 10% and 1% respectively for gaining the strongest UC emission. Subsequently, Ca^{2+} is employed as the surrogate ion for the aim of improving the UC performance of $BaWO_4$:10% Yb^{3+}/1% Er^{3+}. As illustrated in Fig. 2(c), the green UC intensity of the samples is effectively promoted by a factor of 6.5 times as the concentration of Ca^{2+} increases from 0 to 5%, and then gradually diminished with the continuing rise in Ca^{2+} concentration due to the appearance of mixed $CaWO_4$. In addition, $BaWO_4$:10% Yb^{3+}/1% Er^{3+}/5% Ca^{2+} also shows much stronger green UC intensity (2.3 times) than the pure $CaWO_4$ powders doped with the corresponding optimal Yb^{3+} and Er^{3+} concentration, as presented in Fig. S1 (ESI†).

Eu^{3+} has been proved to be a favorable probe for the local structure around rare-earth ions, in which its characteristic electric dipole transition $^5D_0 \rightarrow {}^7F_2$ and magnetic dipole transition $^5D_0 \rightarrow {}^7F_1$ are used as the responders. Since electric dipole transition and magnetic dipole transition are sensitive and insensitive to the crystal field symmetry respectively, their intensity ratio can clearly reveal the evolution of local symmetry around the luminescent centers.[26] Therefore, a series of $BaWO_4$:2% Eu^{3+} doped with the same Ca^{2+} concentration as used in the previous section are synthesized. As shown in Fig. 2(d), several typical emission bands of Eu^{3+} are observed in the photoluminescence (PL) spectra under the excitation of 464 nm wavelength, including $^5D_0 \rightarrow {}^7F_1$ transition at 590 nm, $^5D_0 \rightarrow {}^7F_2$ transition at 615 nm, $^5D_0 \rightarrow {}^7F_3$ transition at 654 nm

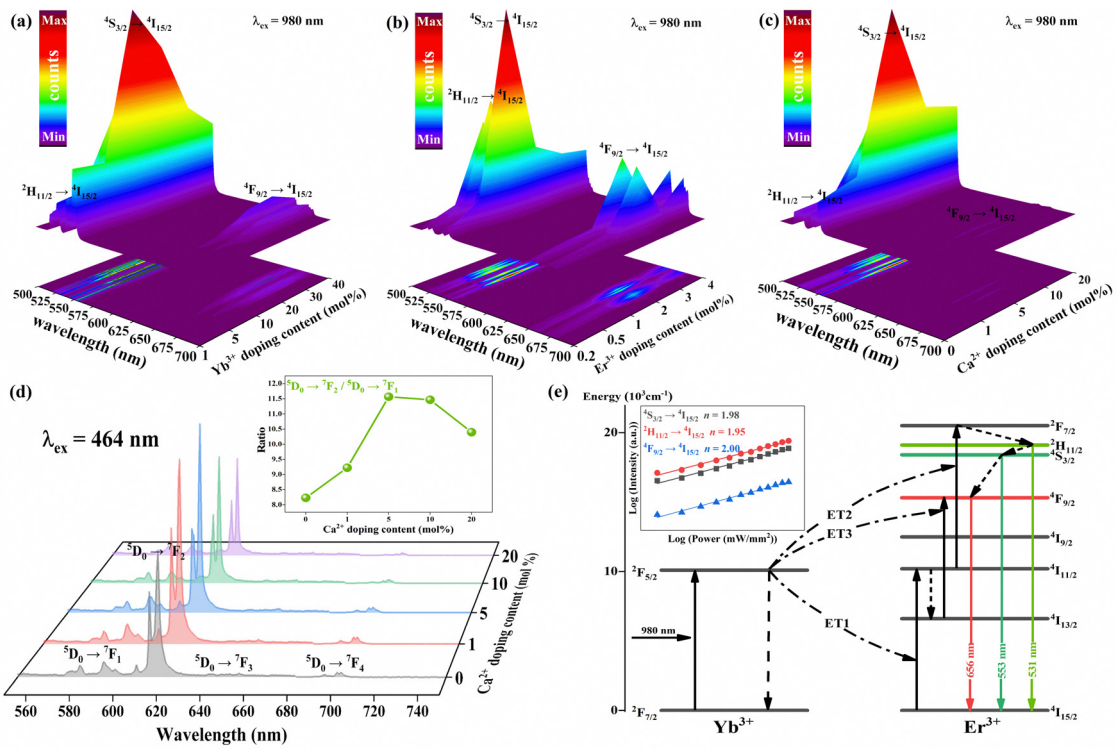

Fig. 2 UC spectra of (a) $BaWO_4$:x% Yb^{3+}/1% Er^{3+}, (b) $BaWO_4$:10% Yb^{3+}/y% Er^{3+} and (c) $BaWO_4$:10% Yb^{3+}/1% Er^{3+}/z% Ca^{2+}. (d) PL spectra of $BaWO_4$:x% Ca^{2+}/2% Eu^{3+} along with the intensity ratio of $^5D_0 \rightarrow {}^7F_2$ transition to $^5D_0 \rightarrow {}^7F_1$ transition as a function of Ca^{2+} doping content. (e) Possible ET processes in $BaWO_4$:10% Yb^{3+}/1% Er^{3+}/5% Ca^{2+}, the inset is the pump power density dependence of the $^2H_{11/2}/{}^4S_{3/2} \rightarrow {}^4I_{15/2}$ and $^4F_{9/2} \rightarrow {}^4I_{15/2}$ transition.

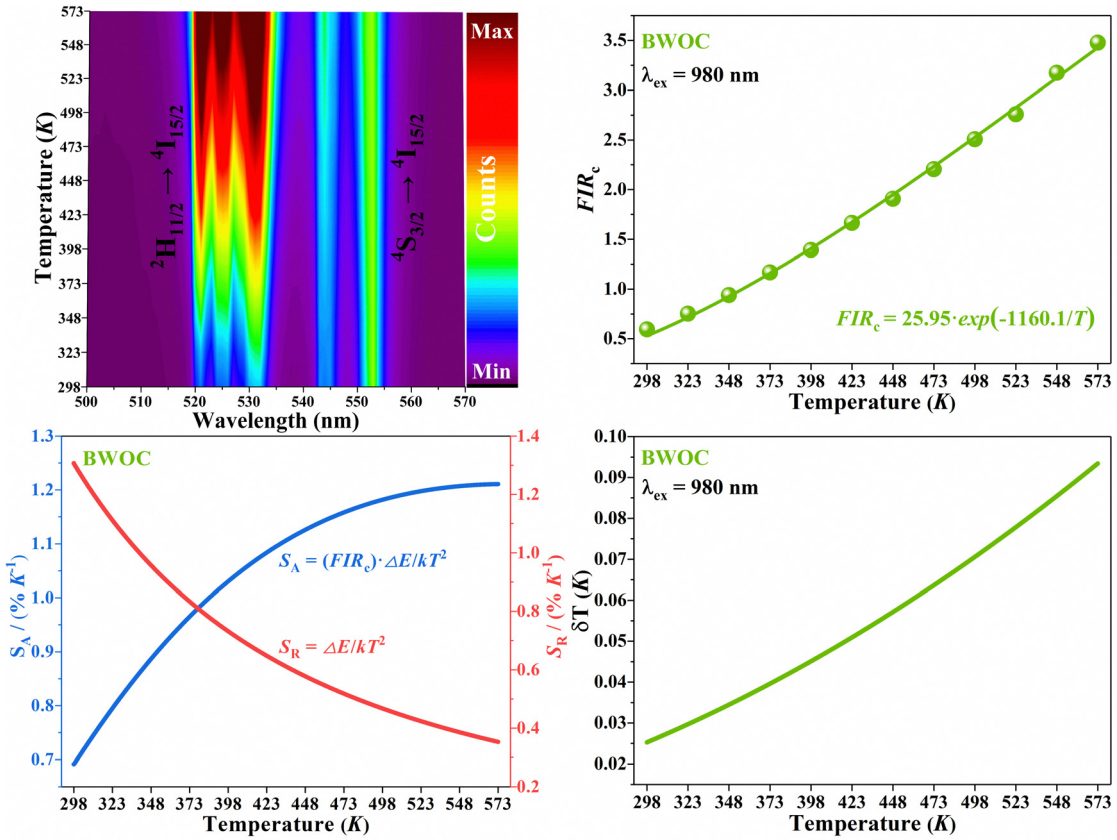

Fig. 3 Temperature-dependent (a) green UC spectra normalized at 553 nm and (b) FIR between $^2H_{11/2} \rightarrow {}^4I_{15/2}$ and $^4S_{3/2} \rightarrow {}^4I_{15/2}$ transition as well as the corresponding temperature sensing (c) sensitivity and (d) resolution in BWOC.

and $^5D_0 \rightarrow {}^7F_4$ transition at 700 nm. More importantly, with the increasing Ca^{2+} concentration, the changing trend of intensity ratio between $^5D_0 \rightarrow {}^7F_2$ and $^5D_0 \rightarrow {}^7F_1$ transition is the same as the emission intensity variation of $BaWO_4$:Yb^{3+}/Er^{3+}/Ca^{2+} shown in Fig. 2(c), strongly demonstrated that the UC intensity enhancement of $BaWO_4$:Yb^{3+}/Er^{3+} is assigned to the destruction of crystal field symmetry through Ca^{2+} doping.

For UC luminescence, the relationship between UC intensity (I) and pump power density (p) can be written as

$$I \propto P^n, \quad (1)$$

where n is the required NIR photon number for emitting one ultraviolet or visible photon. The inset of Fig. 2(e) depicts the pump power density dependence of green and red UC emission in $BaWO_4$:10% Yb^{3+}/1% Er^{3+}/5% Ca^{2+}, from which the n values are calculated to be 1.95 for $^2H_{11/2} \rightarrow {}^4I_{15/2}$ transition, 1.98 for $^4S_{3/2} \rightarrow {}^4I_{15/2}$ transition and 2.00 for $^4F_{9/2} \rightarrow {}^4I_{15/2}$ transition respectively, verifying they are all double-photon processes.

Based on the above analysis, the UC mechanisms in the present sample can be sketched. As presented in Fig. 2(e), 980 nm photons are mainly absorbed by the unexcited Yb^{3+} ions. Then, the Er^{3+} ions at the ground state can receive energy from the excited Yb^{3+} ions through energy transfer (ET) process ET1, giving rise to the population of the $^4I_{11/2}$ level. The Er^{3+} ions at $^4I_{11/2}$ level can be pumped to $^2H_{11/2}$/$^4S_{3/2}$ levels through an ET2 process followed by a series of nonradiative relaxation (NR) processes from the $^4F_{7/2}$ level, resulting in green UC emission. Moreover, the Er^{3+} ions at the $^4I_{11/2}$ level can also be deexcited nonradiatively to the $^4I_{13/2}$ level and then realize the population of the red emitting level $^4F_{9/2}$ *via* the ET3 process. Beyond that, the population of the Er^{3+}:$^4F_{9/2}$ state can be accomplished by the NR process from Er^{3+}:$^2H_{11/2}$/$^4S_{3/2}$ states.

Temperature sensing properties

The temperature sensing properties of $BaWO_4$:10% Yb^{3+}/1% Er^{3+}/5% Ca^{2+} (BWOC) are investigated based on the thermally coupled $^2H_{11/2}$ and $^4S_{3/2}$ states of Er^{3+} ions. As exhibited in Fig. 3(a) and Fig. S2 (ESI†), although the absolute intensity of overall green UC of Er^{3+} is decreased as the temperature increases from 298 K to 573 K, the intensity of $^2H_{11/2} \rightarrow {}^4I_{15/2}$ transition is significantly enhanced relative to $^4S_{3/2} \rightarrow {}^4I_{15/2}$ transition, caused by the thermal excitation from the lower state $^4S_{3/2}$ to the upper state $^2H_{11/2}$. Actually, the relationship of their FIR values and the corresponding temperature obeys the Boltzmann distribution law:

$$\mathrm{FIR} = I_2/I_1 = B \cdot \exp(-\Delta E/kT), \quad (2)$$

here, I_1 and I_2 denote the emission intensity of the lower and upper energy level, k is the Boltzmann's constant and T represents the absolute temperature. B is a temperature-

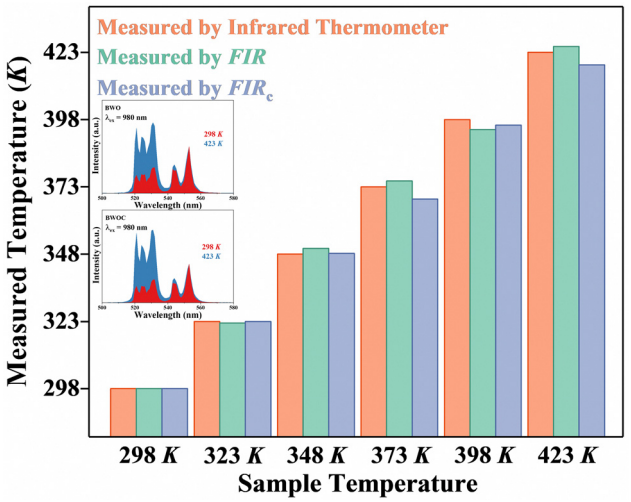

Fig. 4 The sample temperature obtained by FIR technology and infrared thermometer. The insets show the UC spectra of BWO and BWOC collected at 298 K and 423 K.

independent constant. Therefore, as shown in Fig. 3(b), the fitting function of temperature-dependent FIR_c can be calculated as follows:

$$FIR_c = 25.95 \cdot \exp(-1160.1/T), \quad (3)$$

from which the energy gap (ΔE) between the $^2H_{11/2}$ and the $^4S_{3/2}$ state is obtained to be 807 cm^{-1}, close to the value 749 cm^{-1} calculated from the spectra. The error of ΔE between its fitting value and calculated value is derived from the enhancement of the multi-phonon relaxation and ET processes at high temperature.[27] The fitting degree R^2 of FIR_c is 0.9999.

The performance of FIR-based optical thermometers can be well evaluated by absolute sensitivity (S_A) and relative sensitivity (S_R), which can be defined as follows:

$$S_A = |d(FIR)/dT| = FIR \cdot (\Delta E/K_B \cdot T^2), \quad (4)$$

$$S_R = |d(FIR)/(FIR)dT| = \Delta E/(K_B \cdot T^2). \quad (5)$$

As presented in Fig. 3(c), the S_A curve goes up from the initial temperature and reaches its highest value 1.21% K^{-1} at 573 K. Inversely, the S_R shows its maximal value 1.31% K^{-1} at the beginning temperature and then drops to 0.35% K^{-1} with the increasing temperature. Meanwhile, temperature resolution (δT) is another key parameter of optical thermometers, determined by the formula as follows:

$$\delta T = (\delta FIR/FIR) \cdot (1/S_R). \quad (6)$$

Here, δFIR/FIR represents the relative uncertainty of the FIR values, which is primarily associated with the testing equipment. This value is calculated to be 0.033% due to the high accuracy of the spectrometer used in our work. As depicted in Fig. 3(d), the δT curve of BWOC exhibits an increase from 0.025 K to 0.093 K when the temperature rises. Evidently, the δT value remains lower than 0.1 K, revealing the excellent performance of the present thermometer in temperature sensing. Beyond that, the BWOC exhibits outstanding repeatability for temperature sensing, as presented in Fig. S3 (ESI†). The temperature sensing properties of $BaWO_4$:10% Yb^{3+}/1% Er^{3+} (BWO) are also studied, as shown in Fig. S4 (ESI†). Based on the above equations, its optimal S_A, S_R and δT are calculated to be 1.22% K^{-1}, 1.23% K^{-1} and 0.027 K respectively, similar to the corresponding values of BWOC, resulting from the unavailability of Ca^{2+} doping for changing the ΔE between $^2H_{11/2}$ and $^4S_{3/2}$ states.

To verify the accuracy of BWO and BWOC for temperature sensing, FIR technology and infrared thermometer are simultaneously employed to detect the sample temperature. The relevant diagram of the experimental setup is provided in Fig. S5 (ESI†), similar to that used by Guo's group.[28] Firstly, the temperature of the heated sample is measured by an infrared thermometer and the obtained value is regarded as the actual temperature. Then, the corresponding UC spectra of the samples are also collected and used for temperature calculation based on FIR technology. As exhibited in Fig. 4, the sample temperatures obtained from FIR and FIR_c are all close to the actual temperature, manifesting the feasibility of BWO and BWOC as the optical thermometers.

Table 1 presents a compilation of typical optical thermometers utilizing Er^{3+} as the thermometric probe, accompanied by their respective parameters. Compared with the different oxide and fluoride temperature sensors, such as BaY_2O_4:Yb^{3+}/Er^{3+}, $Ca_3Al_2O_6$:Yb^{3+}/Er^{3+}, $Ba_4Y_3F_{17}$:Yb^{3+}/Er^{3+}, β-$NaLuF_4$:Yb^{3+}/Er^{3+} and so on, BWOC shows the largest S_A and S_R values. Combined with its intense green UC emission under the excitation of 980 nm wavelength, BWOC can be considered as a promising candidate for optical thermometry.

Table 1 Various FIR-based optical thermometers and their key parameters

Materials	Dopant	EX (nm)	Temperature (K)	S_A (% K^{-1})	S_R (% K^{-1})	Ref.
$BaWO_4$	$Yb^{3+}/Er^{3+}/Ca^{2+}$	980	298–573	1.21	1.31	This work
BaY_2O_4	Yb^{3+}/Er^{3+}	980	298–573	0.19	—	29
$Ca_3Al_2O_6$	$Yb^{3+}/Er^{3+}/Mg^{2+}$	980	298–573	—	0.78	30
CaO-Y_2O_3	Yb^{3+}/Er^{3+}	980	298–573	0.07	0.67	31
$GdZnTiO_6$	Yb^{3+}/Er^{3+}	980	298–573	0.90	—	32
Gadolinium gallium garnet (GGG)	Yb^{3+}/Er^{3+}	980	300–973	0.41	1.19	33
$Ba_4Y_3F_{17}$	Yb^{3+}/Er^{3+}	980	300–660	—	1.13	34
$K_{0.3}Bi_{0.7}F_{2.4}$	Yb^{3+}/Er^{3+}	980	323–523	0.58	1.08	35
β-$NaLuF_4$	Yb^{3+}/Er^{3+}	980	300–773	—	1.24	36

Conclusions

In summary, the green UC intensity of Yb^{3+}/Er^{3+} codoped $BaWO_4$ is strongly enhanced by a factor of 6.5 times. Such a significant improvement is realized by the destruction of local symmetry around the luminescent centers through Ca^{2+} doping, which has been successfully proved by structural probe Eu^{3+} ions. The experiments also indicated that excellent temperature sensing performance can be obtained in $BaWO_4$:$Yb^{3+}/Er^{3+}/Ca^{2+}$ based on the FIR between the thermally coupled $^2H_{11/2}$ and $^4S_{3/2}$ states of Er^{3+} ions. The optimal S_A and S_R of $BaWO_4$:$Yb^{3+}/Er^{3+}/Ca^{2+}$ is 1.21% K^{-1} and 1.31% K^{-1}, outperforming the majority of the same type optical thermometers. Meanwhile, the δT of the present thermometer remains lower than 0.1 K within the temperature range from 298 K to 573 K. All of the data indicate that a high-performance temperature sensing can be achieved in $BaWO_4$:$Yb^{3+}/Er^{3+}/Ca^{2+}$ along with strong green UC emission.

Conflicts of interest

There are no conflicts to declare.

Acknowledgements

This work is financially supported by the National Natural Science Foundation of China (11704054, 12004062, and 52104392), the Natural Science Foundation of Chongqing (CSTB2022NSCQ-MSX0366 and csct2021jcyj-msxmX0578) and the Science and Technology Research Program of Chongqing Municipal Education Commission (KJZD-K202300612, KJQN202100615, and KJQN202100639).

References

1 B. Zheng, J. Fan, B. Chen, X. Qin, J. Wang, F. Wang and X. Liu, *Chem. Rev.*, 2022, **122**(6), 5519–5603.
2 K. Kumar, N. Vijayalakshmi and J. Choi, *Inorg. Chem.*, 2019, **58**(3), 2001–2011.
3 Z. Yin, H. Li, W. Xu, S. B. Cui, D. L. Zhou, X. Chen, Y. S. Zhu, G. S. Qin and H. W. Song, *Adv. Mater.*, 2016, **28**, 2518–2525.
4 V. Maresh, V. Adusumalli, Y. I. Park and N. Lee, *Mater. Today Chem.*, 2022, **23**, 100752.
5 Z. J. Wang, S. B. Lin, Y. J. Liu, J. Hou, X. Y. Xu, X. Zhao and B. Y. Wei, *Nanomaterial*, 2022, **12**(19), 3288.
6 Z. Wang, X. S. Li, S. Y. Yin, X. Y. Guo and W. P. Qin, *Funct. Mater. Lett.*, 2022, **15**(02), 2251013.
7 W. Zhou, J. Yang, X. L. Jin, Y. Peng and J. Luo, *J. Lumin.*, 2022, **246**, 118807.
8 H. C. Huang, M. H. Yuan, Z. Y. Xing, W. D. Cui, T. C. Yu, S. Hu, G. M. Zhao, C. Guo and K. Han, *J. Mater. Chem. C*, 2022, **10**(42), 15897–15905.
9 S. Bastani, M. Jalili, M. Ghahari and P. Banihashem, *Pigm. Resin Technol.*, 2023, **52**(5), 545–551.
10 W. Zhou, J. Yang, X. L. Jin, Y. Peng and J. Luo, *J. Lumin.*, 2022, **252**, 119275.
11 W. Zhou, J. Yang, X. L. Jin, Y. Peng and J. Luo, *Chin. Phys. Lett.*, 2023, **810**, 140198.
12 L. X. Peng, C. W. Wang, L. P. Li, F. Qin and Z. G. Zhang, *Opt. Lett.*, 2022, **47**(23), 6249–6252.
13 Y. H. Zhang, Y. B. Guo, X. K. Zheng, P. C. Wang and H. Liu, *Physica B*, 2023, **649**, 414467.
14 Y. H. Zhang, N. Zhang, P. C. Wang, X. K. Zheng, Y. B. Guo and H. Liu, *Mater. Today Commun.*, 2022, **33**, 104589.
15 H. Liu, X. K. Jian, M. T. Liu, B. Wang, K. L. Wang and Y. H. Zhang, *Spectrochim. Acta, Part A*, 2022, **277**, 121284.
16 W. Xu, Z. G. Zhang and W. W. Cao, *Opt. Lett.*, 2012, **37**, 4865.
17 Y. H. Zhang, K. L. Wang, M. T. Liu, G. Y. Bai, X. K. Jian and H. Liu, *Optik*, 2021, **242**, 167277.
18 J. B. Huang, Q. F. Li, J. Wang, L. Jin, B. S. Tian, C. Y. Li, Y. R. Shi, Z. L. Wang and J. H. Hao, *Dalton Trans.*, 2018, **47**(26), 8611–8618.
19 A. K. Dey, B. Samanta, P. Bhaumik, S. Manna, A. Halder, T. K. Ghosh, T. K. Parya and U. K. Ghorai, *J. Lumin.*, 2019, **211**, 251–257.
20 L. F. Xu, J. Q. Liu, L. Pei, Y. Xu and Z. G. Xia, *J. Mater. Chem. C*, 2019, **7**(20), 6112–6119.
21 H. Zhang, S. L. Zhao, X. L. Wang, X. T. Ren, J. T. Ye, L. H. Huang and S. Q. Xu, *J. Mater. Chem. C*, 2019, **7**, 15007–15013.
22 A. Dubey, A. K. Soni, A. Kumari, R. Dey and V. K. Rai, *J. Alloys Compd.*, 2017, **693**, 194–200.
23 K. Zhang, L. P. Tong, Y. F. Ma, J. F. Wang, Z. C. Xia and Y. B. Han, *J. Alloys Compd.*, 2019, **781**, 467–472.
24 Y. Li, G. F. Wang, K. Pan, N. Y. Fan, S. Liu and L. Feng, *RSC Adv.*, 2013, **3**, 1683–1686.
25 D. G. Yin, C. C. Wang, J. Ouyang, K. L. Song, B. Liu, X. Z. Cao, L. Zhang, Y. L. Han, X. Long and M. H. Wu, *Dalton Trans.*, 2014, **43**, 12037–12043.
26 H. Suo, X. Q. Zhao, Z. Y. Zhang, R. Shi, Y. F. Wu, J. M. Xiang and C. F. Guo, *Nanoscale*, 2018, **10**, 9245–9251.
27 X. Wang, Y. Wang, Y. Bu, X. Yan, J. Wang, P. Cai, T. Vu and H. J. Seo, *Sci. Rep.*, 2017, **7**, 1–9.
28 H. Suo, X. Q. Zhao, Z. Y. Zhang, Y. F. Wu and C. F. Guo, *ACS Appl. Mater. Interfaces*, 2018, **10**, 39912–39920.
29 G. T. Xiang, X. T. Liu, Q. Xia, S. Jiang, X. J. Zhou, L. Li, Y. Jin, L. Ma, X. J. Wang and J. H. Zhang, *Inorg. Chem.*, 2020, **59**(15), 11054–11060.
30 X. F. Wang, Y. Wang, L. S. Jin, Y. Y. Bu, X. L. Yang and X. H. Yan, *J. Alloys Compd.*, 2019, **773**, 393–400.
31 G. T. Xiang, X. T. Liu, W. Liu, B. Wang, Z. Liu, S. Jiang, X. J. Zhou, L. Li, Y. Jin and J. H. Zhang, *J. Am. Chem. Soc.*, 2020, **103**(4), 2540–2547.
32 J. S. Liao, L. Y. Kong, M. H. Wang and J. X. Huang, *ECS J. Solid State Sci. Technol.*, 2019, **8**(11), R149.
33 M. Erdem, H. Örücü, S. B. Canturk and G. Eryürek, *ACS Appl. Nano Mater.*, 2021, **4**(7), 7162–7171.
34 Y. Li, W. M. Wang, Y. Pan, H. M. Chen, Q. W. Cao and X. T. Wei, *CrystEngComm*, 2020, **22**(38), 6302–6309.
35 X. L. Gao, F. Song, D. D. Ju, A. H. Zhou, A. Khan, Z. Y. Chen, X. Sang, M. Feng and L. S. Liu, *CrystEngComm*, 2020, **22**(42), 7066–7074.
36 X. Y. Li, L. Y. Yang, Y. W. Zhu, J. S. Zhong and D. Q. Chen, *RSC Adv.*, 2019, **9**(14), 7948–7954.